Marijn Nijenhuis
Precision Engineering,
University of Twente,
Enschede 7522 NB, The Netherlands
e-mail: m.nijenhuis@utwente.nl

J. P. Meijaard
Precision Engineering,
University of Twente,
Enschede 7522 NB, The Netherlands;
Olton Engineering Consultancy,
Enschede 7522 NB, The Netherlands
e-mail: j.p.meijaard@utwente.nl

Dhanushkodi Mariappan
Precision Systems Design Lab,
Mechanical Engineering,
University of Michigan,
Ann Arbor, MI 48109
e-mail: dhanush@umich.edu

Just L. Herder
Precision Engineering,
University of Twente,
Enschede 7522 NB, The Netherlands
e-mail: j.l.herder@utwente.nl

Dannis M. Brouwer
Precision Engineering,
University of Twente,
Enschede 7522 NB, The Netherlands
e-mail: d.m.brouwer@utwente.nl

Shorya Awtar[1]
Precision Systems Design Lab,
Mechanical Engineering,
University of Michigan,
Ann Arbor, MI 48109
e-mail: awtar@umich.edu

An Analytical Formulation for the Lateral Support Stiffness of a Spatial Flexure Strip

A flexure strip has constraint characteristics, such as stiffness properties and error motions, that govern its performance as a basic constituent of flexure mechanisms. This paper presents a new modeling approach for obtaining insight into the deformation and stiffness characteristics of general three-dimensional flexure strips that exhibit bending, shear, and torsion deformation. The approach is based on the use of a discretized version of a finite (i.e., nonlinear) strain spatial beam formulation for extracting analytical expressions that describe deformation and stiffness characteristics of a flexure strip in a parametric format. This particular way of closed-form modeling exploits the inherent finite-element assumptions on interpolation and also lends itself for numeric implementation. As a validating case study, a closed-form parametric expression is derived for the lateral support stiffness of a flexure strip and a parallelogram flexure mechanism. This captures a combined torsion–bending dictated geometrically nonlinear effect that undermines the support bearing stiffness when the mechanism moves in the intended degree of freedom (DoF). The analytical result is verified by simulations and experimental measurements. [DOI: 10.1115/1.4035861]

1 Introduction

Flexure strips are common building blocks of flexure mechanisms that guide motion by means of elastic deformation [1,2]. Although these mechanisms provide a limited range of motion, this motion is deterministic and repeatable. These attributes make flexure mechanisms useful in precision manipulation designs.

A flexure strip can be regarded as a constraint element [3]: when connected to two rigid bodies, one at each end, the flexure strip constrains certain relative motions. This function is dictated by its elastic properties and a consequence of its slender geometry: typically, one dimension (i.e., the thickness) is at least an order of magnitude smaller than the length and width.

Figure 1 depicts a flexure strip that is clamped on the left side. The right side exhibits relatively small stiffness along certain directions, characterized as degrees-of-freedom (DoF), and relatively large stiffness along other directions, characterized as degrees of constraint (DoC) or support bearing directions [4]. Considering the motion of the free end with respect to the fixed, the translational y-direction and the rotational x- and z-directions are DoF; the rotational y-direction and translational x- and z-directions are DoC. This translational z-direction is also referred to as the lateral support direction in the present work. While an ideal constraint element would provide zero stiffness along the DoF and infinite stiffness along the DoC, the flexure strip clearly deviates from the idealized constraint with only a limited, even though large, ratio between DoF and DoC stiffness.

Several components contribute to DoC compliance of flexure strips: in addition to common linear elastic contributions from bending, shear, and elongation, a nonlinear dependency on

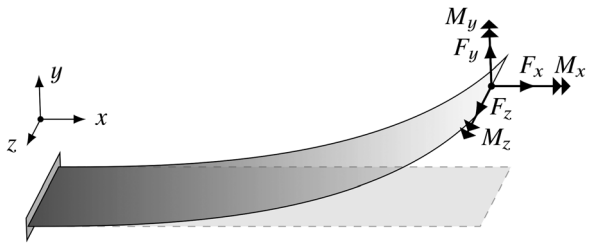

Fig. 1 Deformed fixed–free flexure strip with general end-load of forces F_x, F_y, F_z, and moments M_x, M_y, M_z

[1]Corresponding author.

Contributed by the Design Automation Committee of ASME for publication in the Journal of Mechanical Design. Manuscript received July 1, 2016; final manuscript received January 11, 2017; published online March 20, 2017. Assoc. Editor: Nam H. Kim.

displacement is present. Such a geometric stiffness nonlinearity causes an unwanted DoC stiffness decrease when the strip deformation along a DoF increases [5,6]. This stiffness component is a manifestation of the trade-off that exists between DoF and DoC performance characteristics [4]. When seeking to synthesize and optimize flexure mechanisms, a designer benefits from parametric insight into the relation between performance and design variables, to achieve an objective compromise. A designer needs to know how the choice of material, dimensions, and loads (forces and moments) acting on the ends affects the performance characteristics of the flexure strip, in order to exploit its behavior in mechanism designs. Such design insights are the topic of this work.

While the finite-element method generally gives accurate results, it does so for only a single configuration at a time, without offering direct insight into the relevant design parameters and their sensitivity. This establishes the need for mathematical, closed-form relations that express the performance of building blocks in terms of design parameters. In particular, the flexure strip deforming spatially (in 3D) due to a general end-load (as depicted in Fig. 1) deserves treatment because of its use in practical applications.

In literature, various analytical models can be found that work toward this objective. In structural mechanics, the subject of beam and plate theory encompasses structures shaped like typical flexure strips. Research results in this field have accumulated over centuries and resulted in a vast body of literature. For a comprehensive overview in the context of flexure mechanisms, the reader is referred to Ref. [7].

To establish some context for the present work, we provide a sampling of relevant literature on flexure strip models. The beam constraint model [4,8] describes the constraint behavior of planar (2D) flexure strips that deform solely in the (x, y)-plane of Fig. 1. In a compact closed-form parametric format, it captures relevant nonlinearities with sufficient accuracy for a practical load and displacement range. The presence of geometric nonlinearities that cause a decrease in DoC quality with increased DoF motion is shown between the translational x-direction DoC and y-direction DoF. While the beam constraint model has been extended to spatial (3D) deformation [9], it is limited to slender beamlike flexures that, unlike flexure strips, have two comparable cross-sectional principal area moments of inertia. Although pseudorigid body models have been extended to 3D [10,11], they are fundamentally not parametric in the applied loads and preclude effects that stem from the distributed compliance of flexure elements. Limited to the case of a specific embodiment of a parallelogram flexure mechanism that deforms in 3D, Brouwer et al. [5] presented accurate analytical expressions for the stiffness in various constraint directions, taking into account shear compliance and constrained cross-sectional warping.

The present investigation does not contribute any new mechanics theory; instead, a novel contribution of this paper is a new approach for extracting closed-form expressions pertinent to flexure design, from an *existing* mechanics formulation. Ultimately, this supports further development of comprehensible models that aid flexure mechanism designers. A key new idea of this approach is to perform *analytical* calculations by means of the *discretized* version of a continuum beam model. While conventionally used for numeric computations, the nature of the discretized model here facilitates analytical calculations by exploiting the inherent finite-element assumptions on interpolation.

To convey this new approach, this paper provides both the foundation (an overview of the adopted model) and a validation (a rederivation of prior art results and a new experiment). The novel contributions of this paper further include a closed-form expression for the lateral support stiffness of a flexure strip as a function of its transverse displacement and a spatial end-load (i.e., involving torsion). The expression explicates the observation that DoC performance, i.e., support bearing stiffness, diminishes when the strip is deflected in the intended DoF. Moreover, via a carefully designed and conducted experiment, this work presents the first direct measurement of the lateral stiffness of a parallelogram flexure mechanism as a function of its transverse displacement. Many factors that adversely affect the measurements have been accounted for, such as unintended sources of compliance in the system, friction/hysteresis/backlash in actuation and sensing, and measurement drift.

The rest of this paper is organized as follows. Section 2 primes the reader with a brief overview of the continuum beam model. Section 3 provides the discretization step and discretized model. Section 4 examines the lateral support stiffness of a flexure strip as a case study. Section 5 validates the closed-form model with an experiment. Section 6 presents the conclusions.

2 Continuum Model

While the general three-dimensional continuum mechanics relations govern the flexure strip behavior of interest, simplifying assumptions are necessary to get the comprehensible model that we aim for. It has been shown that one-dimensional beam theory with some refinements is sufficiently accurate for practical flexure strip geometries, obviating the need for the more complex plate theory [5,7,12]. These refinements account for effects that stem from the platelike behavior of flexure strips with certain geometries, such as the effect of the warping and anticlastic bending constraint. Past experience with the software implementation [13] of this theory has confirmed its capability to numerically predict experimental measurements on flexure mechanisms [14–16]. In this section, we will give a brief overview of a beam model capable of bending, torsion, shear, and elongation deformation, based on Timoshenko's assumptions.

2.1 Kinematic Description of a Deformed Beam. A statically deformed, load-carrying, spatial beam can be represented by a Cosserat rod [17,18], consisting of

(1) the position of the beam's elastic line
(2) the orientation of the cross sections

This beam representation is convenient, because it adds the notion of a rotation field—unlike general elasticity theory, which only considers a displacement field.

The fixed–free beam in Fig. 2(*a*) has an undeformed length L and independent coordinate $s \in [0, L]$ along the elastic line. The orientation of a cross section at an arbitrary position on the elastic line is given by an orthonormal set of three vectors

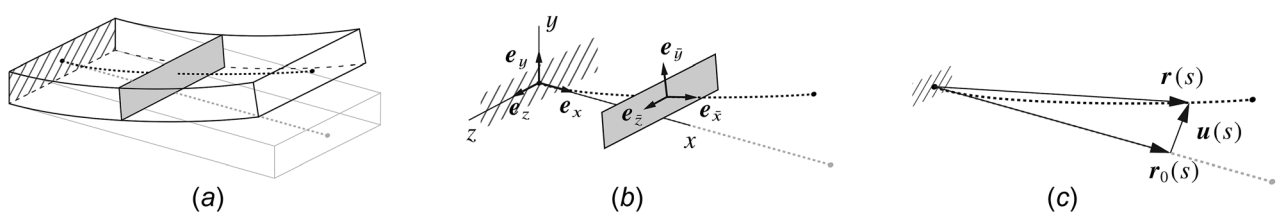

Fig. 2 (*a*) Deformed configuration of a flexure strip modeled as a beam (thickness exaggerated), (*b*) orientation of a single cross section, and (*c*) position of a point on the elastic line

- $\boldsymbol{e}_{\bar{x}}$, pointing in the average [19] normal direction to the cross section
- $\boldsymbol{e}_{\bar{y}}$ and $\boldsymbol{e}_{\bar{z}}$, pointing in the direction of the principal axes of the cross section, hence spanning the cross-sectional plane

The vectors $\boldsymbol{e}_{\bar{x}}$, $\boldsymbol{e}_{\bar{y}}$, and $\boldsymbol{e}_{\bar{z}}$ (with overbar) thus represent a *local* frame (Fig. 2(*b*)), dependent on s, that defines the orientation of each cross section. The origin of this local frame coincides with the centroid of the cross section. For the purpose of this work, the left end of the beam ($s=0$) is considered fixed, so that the cross-sectional orientation vectors at $s=0$ can be used as *fixed* coordinate frame vectors $\boldsymbol{e}_x$, $\boldsymbol{e}_y$, and $\boldsymbol{e}_z$ (without overbar), i.e., $[\boldsymbol{e}_x \quad \boldsymbol{e}_y \quad \boldsymbol{e}_z] := [\boldsymbol{e}_{\bar{x}} \quad \boldsymbol{e}_{\bar{y}} \quad \boldsymbol{e}_{\bar{z}}]$ at $s=0$, for fixed coordinate system x, y, z. All vectors are resolved in this coordinate system unless noted otherwise. Then, the cross-sectional orientation in the deformed configuration can be defined by the transformation

$$\underbrace{[\boldsymbol{e}_{\bar{x}} \quad \boldsymbol{e}_{\bar{y}} \quad \boldsymbol{e}_{\bar{z}}]}_{\substack{\text{deformed}\\ \text{cross section}}} = \boldsymbol{R}(s) \underbrace{[\boldsymbol{e}_x \quad \boldsymbol{e}_y \quad \boldsymbol{e}_z]}_{\substack{\text{undeformed}\\ \text{cross section}}} \tag{1}$$

where $\boldsymbol{R}(s)$ is a rotation matrix.

The coordinates of the elastic line in the fixed frame are expressed (Fig. 2(*c*)) as

$$\boldsymbol{r}(s) = \boldsymbol{r}_0(s) + \boldsymbol{u}(s) = s\boldsymbol{e}_x + [\boldsymbol{e}_x \quad \boldsymbol{e}_y \quad \boldsymbol{e}_z] \begin{bmatrix} u_x(s) \\ u_y(s) \\ u_z(s) \end{bmatrix} \tag{2}$$

where vector $\boldsymbol{r}_0(s)$ denotes the undeformed (straight) elastic line, and $\boldsymbol{u}(s) = [u_x, u_y, u_z]^{\mathrm{T}}$ denotes the deflection.

The cross-sectional orientation can be expressed by a number of parameters, such as the components of $\boldsymbol{e}_{\bar{x}}, \boldsymbol{e}_{\bar{y}}, \boldsymbol{e}_{\bar{z}}$, the components of $\boldsymbol{R}$, or some parameterization of $\boldsymbol{R}$ [20]. We will choose the three Tait–Bryan angles ϕ_x, ϕ_y, and ϕ_z to represent successive, intrinsic, active rotation about the x-, y-, and z-axes, according to

$$\boldsymbol{R}(s) = \begin{bmatrix} \mathrm{c}\phi_z & -\mathrm{s}\phi_z & 0 \\ \mathrm{s}\phi_z & \mathrm{c}\phi_z & 0 \\ 0 & 0 & 1 \end{bmatrix} \begin{bmatrix} \mathrm{c}\phi_y & 0 & \mathrm{s}\phi_y \\ 0 & 1 & 0 \\ -\mathrm{s}\phi_y & 0 & \mathrm{c}\phi_y \end{bmatrix} \begin{bmatrix} 1 & 0 & 0 \\ 0 & \mathrm{c}\phi_x & -\mathrm{s}\phi_x \\ 0 & \mathrm{s}\phi_x & \mathrm{c}\phi_x \end{bmatrix} \tag{3}$$

where c and s are short for cosine and sine, and $\boldsymbol{\phi}(s) = [\phi_x, \phi_y, \phi_z]^{\mathrm{T}}$.

Six functions, viz., the orientation parameters $\boldsymbol{\phi}(s)$ and the elastic line $\boldsymbol{r}(s)$, fully define the deformed configuration of the fixed–free beam.

2.2 Strain and Curvature Measures. To accurately capture typical flexure mechanism deformation, linearized (infinitesimal) strains are inadequate. Suitable measures that characterize *finite* deformation of the Cosserat rod representation are given by [21]

$$\begin{bmatrix} \gamma_{\bar{x}} \\ \gamma_{\bar{y}} \\ \gamma_{\bar{z}} \end{bmatrix} = \boldsymbol{R}^{\mathrm{T}}(\boldsymbol{r}' - \boldsymbol{e}_{\bar{x}}), \qquad \begin{bmatrix} 0 & -\kappa_{\bar{z}} & \kappa_{\bar{y}} \\ \kappa_{\bar{z}} & 0 & -\kappa_{\bar{x}} \\ -\kappa_{\bar{y}} & \kappa_{\bar{x}} & 0 \end{bmatrix} = \boldsymbol{R}^{\mathrm{T}}\boldsymbol{R}'$$

and collected in $\boldsymbol{\gamma} = [\gamma_{\bar{x}}, \gamma_{\bar{y}}, \gamma_{\bar{z}}]^{\mathrm{T}}$ and $\boldsymbol{\kappa} = [\kappa_{\bar{x}}, \kappa_{\bar{y}}, \kappa_{\bar{z}}]^{\mathrm{T}}$. A prime denotes differentiation with respect to s. These nonlinear expressions are constructed to ensure consistency with the exact beam equilibrium equations and energetic duality to the internal forces and internal moments [22].

With the parameterization of $\boldsymbol{r}$ and $\boldsymbol{R}$ in Eqs. (2) and (3), they can be given an interpretation. Using a second-order series expansion of $\boldsymbol{R}$, the strains are as follows:

$$\begin{aligned} \gamma_{\bar{x}} &\approx u_x' - \phi_y\left(u_z' + \frac{1}{2}\phi_y\right) + \phi_z\left(u_y' - \frac{1}{2}\phi_z\right) \\ &\quad \text{(axial strain)} \\ \gamma_{\bar{y}} &\approx u_y' - \phi_z + \phi_x\left(u_z' + \phi_y\right) - \phi_z u_x' \\ &\quad \text{(transverse shear } (\bar{x},\bar{y})\text{-plane)} \\ \gamma_{\bar{z}} &\approx u_z' + \phi_y - \phi_x\left(u_y' - \phi_z\right) + \phi_y u_x' \\ &\quad \text{(transverse shear } (\bar{x},\bar{z})\text{-plane)} \end{aligned} \tag{4a}$$

Three curvature measures are identified as

$$\begin{aligned} \kappa_{\bar{x}} &\approx \phi_x' - \phi_y\phi_z' && \text{specific twist angle} \\ \kappa_{\bar{y}} &\approx \phi_y' + \phi_x\phi_z' && \text{bending curvature } (\bar{x},\bar{z})\text{-plane} \\ \kappa_{\bar{z}} &\approx \phi_z' - \phi_x\phi_y' && \text{bending curvature } (\bar{x},\bar{y})\text{-plane} \end{aligned} \tag{4b}$$

2.3 Constitutive Relations and Internal Loads. In general, a beam cross section is loaded by a force vector $\boldsymbol{N}(s)$ and moment vector $\boldsymbol{M}(s)$. A general constitutive model expresses these internal loads as nonlinear functions of the deformation measures [23]. Common *linear* elastic material behavior is given by

$$\begin{aligned} \boldsymbol{N} &= (EA\gamma_{\bar{x}}, GAk_y\gamma_{\bar{y}}, GAk_z\gamma_{\bar{z}})^{\mathrm{T}} \\ \boldsymbol{M} &= (GJ\kappa_{\bar{x}}, EI_y\kappa_{\bar{y}}, EI_z\kappa_{\bar{z}})^{\mathrm{T}} \end{aligned} \tag{5}$$

where E is Young's modulus, A is the cross-sectional area, G is the shear modulus, k_y and k_z are the shear correction factors, J is Saint-Venant's torsion constant, and I_y and I_z are the area moments of inertia about the principal axes. This particular constitutive model has been used before [14,24,25] and will be adopted in Sec. 3.

2.4 Strain Energy. For elastic materials, the strain energy in terms of the deformation measures $\boldsymbol{\gamma}$ and $\boldsymbol{\kappa}$ is given by

$$P_{\mathrm{cont}} = \int_0^L \sum_i \left(\int_0^{\kappa_i} M_i \mathrm{d}\bar{\kappa}_i + \int_0^{\gamma_i} N_i \mathrm{d}\bar{\gamma}_i \right) \mathrm{d}s \tag{6}$$

where subscript i refers to the ith component of the corresponding vector.

3 Discretized Model

The one-dimensional continuum model is converted to a discrete model of finite size. This has been detailed and implemented as a finite element in numeric software (serving, e.g., as a solver for large problems or as a validation for analytical calculations) in the past [13,21]. This section treats a new presentation of the discretization procedure that emphasizes the continuum model origin and improves clarity in the process of obtaining closed-form expressions, exemplified in Sec. 4 with a case study.

The essence of the discrete beam model is that the characteristic properties (such as deformation and stress state of the beam) are no longer continuous functions of the coordinate along the beam; instead, these properties are given by a set of *discrete variables* that are inferred from *only* the configuration of the beam endpoints.

3.1 Kinematic Description of a Discrete Beam Model. The continuous position $\boldsymbol{r}(s)$ and orientation $\boldsymbol{\phi}(s)$ functions, fully describing a deformed continuous beam, are discretized by only retaining their values at the beam endpoints, i.e., at $s=0$ and $s=L$. These points, referred to as nodes p and q, account for the entire kinematic description of the finite beam element. By considering one side (node p here) of the beam to be fixed in this work, we neglect any rigid-body motion of the finite element and solely focus on its deformation. The only parameters needed to describe the deformation of the resulting *discrete beam model* are the *nodal coordinates* in q:

- the three position coordinates $L+u_x^q$, u_y^q, and u_z^q in node q, given by $\boldsymbol{r}(L)$ from Sec. 2.1
- the three orientation parameters ϕ_x^q, ϕ_y^q, and ϕ_z^q in node q, given by $\boldsymbol{\phi}(L)$ from Sec. 2.1

These six parameters are collected in the nodal coordinate vector

$$\boldsymbol{x} = \left[L+u_x^q,\ u_y^q,\ u_z^q,\ \phi_x^q,\ \phi_y^q,\ \phi_z^q\right]^{\mathrm{T}} \tag{7}$$

3.1.1 Interpolation Between Nodes. Interpolation functions can be used to estimate the position and orientation between nodes p and q. These are based on the solutions of linear analyses of beams and are given by [21,26]

$$\begin{aligned}
u_y(\xi) &= \frac{1}{1+\Phi_y}\begin{bmatrix} u_y^q & L\phi_z^q \end{bmatrix}\begin{bmatrix} 3\xi^2-2\xi^3+\Phi_y\xi \\ -\xi^2+\xi^3+\frac{1}{2}\Phi_y\left(-\xi+\xi^2\right)\end{bmatrix}\\
u_z(\xi) &= \frac{1}{1+\Phi_z}\begin{bmatrix} u_z^q & L\phi_y^q \end{bmatrix}\begin{bmatrix} 3\xi^2-2\xi^3+\Phi_z\xi \\ \xi^2-\xi^3+\frac{1}{2}\Phi_z\left(\xi-\xi^2\right)\end{bmatrix}\\
\phi_y(\xi) &= \frac{1}{1+\Phi_z}\begin{bmatrix} u_z^q & \phi_y^q \end{bmatrix}\begin{bmatrix} 6/L\left(\xi^2-\xi\right) \\ -2\xi+3\xi^2+\Phi_z\xi\end{bmatrix}\\
\phi_z(\xi) &= \frac{1}{1+\Phi_y}\begin{bmatrix} u_y^q & \phi_z^q \end{bmatrix}\begin{bmatrix} 6/L\left(\xi-\xi^2\right) \\ -2\xi+3\xi^2+\Phi_y\xi\end{bmatrix}
\end{aligned} \tag{8}$$

with dimensionless coordinate $\xi=s/L$ and shear factors

$$\Phi_y = \frac{12EI_z}{k_yGAL^2} \quad \text{and} \quad \Phi_z = \frac{12EI_y}{k_zGAL^2}$$

The longitudinal displacement and twist angle are interpolated linearly, i.e., $u_x(\xi)=u_x^q\xi$ and $\phi_x(\xi)=\phi_x^q\xi$.

Despite the linear analysis nature, geometric nonlinearities are accounted for by means of the (discrete equivalent of the) nonlinear finite deformation measures in Eq. (4).

The use of the interpolation functions in Eq. (8) implies that axial loads have no significant contribution to the internal bending moments. To accurately model the effects of axial loads, the interpolation functions in Eq. (8) can be complemented with an additional term [4,27].

3.2 Strain Energy Balance. We now state that the stress state of the discrete beam is characterized by *generalized stresses* $\boldsymbol{\sigma}$. They give rise to a deformed state, characterized by *discrete deformations* $\boldsymbol{\varepsilon}$ that are energy-conjugates of $\boldsymbol{\sigma}$. Consequently, the strain energy of the discrete beam is given by

$$P_{\mathrm{disc}} = \sum_i \int_0^{\varepsilon_i} \sigma_i \mathrm{d}\bar{\varepsilon}_i \tag{9}$$

where subscript i refers to the ith component of the corresponding vector.

The principle relating the discrete model to the continuum model is chosen to be that both contain the same strain energy when subjected to the same nodal loads. Under the assumption of linear constitutive relations, i.e., Eq. (5) for the continuum and $\boldsymbol{\sigma}=\boldsymbol{S}\boldsymbol{\varepsilon}$ for the discrete model with as of yet unknown stiffness matrix $\boldsymbol{S}$, this balance is expressed as

$$\boldsymbol{\sigma}^{\mathrm{T}}\boldsymbol{\varepsilon} = \int_0^L \left(\boldsymbol{M}^{\mathrm{T}}\boldsymbol{\kappa}+\boldsymbol{N}^{\mathrm{T}}\boldsymbol{\gamma}\right)\mathrm{d}s \tag{10}$$

Although up to this point both $\boldsymbol{\sigma}$ and $\boldsymbol{\varepsilon}$ lack a specific definition, Eq. (10) provides the condition that ensures that they are energy-conjugates and consistent with one-dimensional continuum theory. It also shows that, in accordance with its construction, the discrete model contribution (on the left-hand side) does not depend on the material coordinate s.

Table 1 summarizes the various analogous beam properties that have been introduced in the continuous and discrete model. In the remainder of this section, the stress and strain measures will be specified further, along with the appropriate constitutive model.

3.3 Generalized Stresses. In order to specify some relation between the constant generalized stresses $\boldsymbol{\sigma}$ of the discrete model and the internal loads $\boldsymbol{M}(s)$ and $\boldsymbol{N}(s)$ of the continuum model, first, *average* internal loads, independent of s, are defined (denoted by a superscript tilde). They are based on the continuous strain energy for linear material behavior, i.e., the right-hand side of Eq. (10), as

$$\begin{aligned}
\tilde{\boldsymbol{M}}^{\mathrm{T}}\int_0^L \boldsymbol{\kappa}\mathrm{d}s &= \int_0^L \boldsymbol{M}^{\mathrm{T}}\boldsymbol{\kappa}\mathrm{d}s\\
\tilde{\boldsymbol{N}}^{\mathrm{T}}\int_0^L \boldsymbol{\gamma}\mathrm{d}s &= \int_0^L \boldsymbol{N}^{\mathrm{T}}\boldsymbol{\gamma}\mathrm{d}s
\end{aligned} \tag{11}$$

With this strain energy balance, the constants $\tilde{\boldsymbol{M}}$ and $\tilde{\boldsymbol{N}}$ are defined as curvature- and strain-weighted averages of the internal loads. Also, two auxiliary characteristic lengths $\tilde{s}_y$ and $\tilde{s}_z$ are defined

$$\begin{aligned}
\tilde{s}_y\int_0^L \kappa_{\bar{y}}\mathrm{d}s &= \int_0^L \kappa_{\bar{y}}s\mathrm{d}s\\
\tilde{s}_z\int_0^L \kappa_{\bar{z}}\mathrm{d}s &= \int_0^L \kappa_{\bar{z}}s\mathrm{d}s
\end{aligned} \tag{12}$$

as the distance from $s=0$ to the centroid of the $\kappa_{\bar{y}}(s)$ and $\kappa_{\bar{z}}(s)$ diagrams.

3.3.1 Interpretation of Average Internal Loads. An interpretation of the average bending moments $\tilde{M}_y$ and $\tilde{M}_z$ and the auxiliary characteristic lengths $\tilde{s}_y$ and $\tilde{s}_z$ follows from a linear analysis, i.e., for infinitesimal displacements, when the strains and curvatures can be linearized, and load equilibrium can be applied in the undeformed configuration. In that case, the constant torsion moment,

Table 1 Overview of beam properties

Continuum model		Discrete model
$\boldsymbol{r}(s)$	Position	$\boldsymbol{r}(0)$, $\boldsymbol{r}(L)$
$\boldsymbol{R}(s)$	Orientation	$\boldsymbol{R}(0)$, $\boldsymbol{R}(L)$
$\boldsymbol{F}$, $\boldsymbol{T}$	External loads	$\boldsymbol{F}$, $\boldsymbol{T}$
$\boldsymbol{N}(s)$, $\boldsymbol{M}(s)$	Stress measures	$\boldsymbol{\sigma}$
$\boldsymbol{\kappa}(s)$, $\boldsymbol{\gamma}(s)$	Strain measures	$\boldsymbol{\varepsilon}$
$(\boldsymbol{N},\boldsymbol{M})=\boldsymbol{f}_1(\boldsymbol{\kappa},\boldsymbol{\gamma})$	Constitutive model	$\boldsymbol{\sigma}=\boldsymbol{f}_2(\boldsymbol{\varepsilon})$

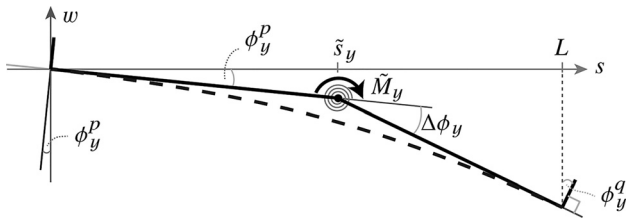

Fig. 3 Interpretation of average bending moment $\tilde{M}_y$ using an imaginary lumped torsion spring

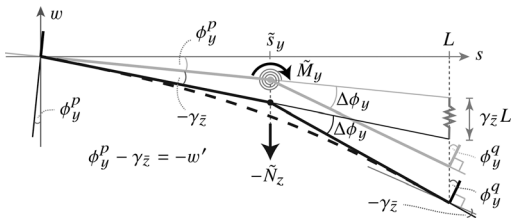

Fig. 4 Interpretation of average bending moment $\tilde{M}_y$ and shear force $\tilde{N}_z$ using imaginary lumped torsional and linear springs

normal force, and shear forces are identical to, respectively, $\tilde{M}_x$, $\tilde{N}_x$, $\tilde{N}_y$, and $\tilde{N}_z$.

Figure 3 shows a beam (dashed) subjected to pure bending in the (x, z)-plane. Its two cross sections at $s=0$ (node p) and $s=L$ (node q) are oriented at ϕ_y^p and ϕ_y^q, respectively. (Angle ϕ_y^p is zero in the current work but nonzero here for visualization purposes.) The bending deformation mechanism is depicted by the two elastic line tangents in nodes p and q that intersect in $s=\tilde{s}_y$ at an angle equal to $\Delta\phi=\phi_y^q-\phi_y^p$ in the absence of shear strain. This way the beam's curvature is essentially concentrated in a point. The strain energy due to this deformation is

$$\int_0^L M_{\bar{y}}\kappa_{\bar{y}}\mathrm{d}s=\tilde{M}_y\int_0^L \kappa_{\bar{y}}\mathrm{d}s\approx\tilde{M}_y\Delta\phi_y$$

using the linear curvature term of Eq. (4). At the tangents intersection $s=\tilde{s}_y$, we therefore imagine a torsion spring that stores this amount of strain energy when rotated by $\Delta\phi_y$ due to average bending moment $\tilde{M}_y$.

When shear deformation is also present, the extra shear strain energy term is

$$\int_0^L N_{\bar{z}}\gamma_{\bar{z}}\mathrm{d}s=\tilde{N}_z\int_0^L \gamma_{\bar{z}}\mathrm{d}s\approx\tilde{N}_z\gamma_{\bar{z}}L \tag{13}$$

where the shear angle is assumed to be constant. Figure 4 depicts both bending and shear deformations. The cross sections still have the same orientation, but now the elastic line tangents in both nodes are offset by the shear angle $\gamma_{\bar{z}}$. Because $\gamma_{\bar{z}}$ is constant (the shear force in a linear analysis does not vary), the tangents still intersect at $\Delta\phi_y$. We therefore consider the beam deformation to occur in two stages:

(1) Curvature due to bending is concentrated in $s=\tilde{s}_y$ and caused by $\tilde{M}_y$. Bending strain energy is represented by a torsion spring rotated by $\Delta\phi_y$.
(2) Shear force $\tilde{N}_z$ is applied in $s=\tilde{s}_y$ and establishes shear angle $\gamma_{\bar{z}}$. Shear strain energy is represented by a linear spring of length $\gamma_{\bar{z}}L$, according to Eq. (13).

This interpretation focuses on deformation in the (x, z)-plane. For deformation in the (x, y)-plane, a similar reasoning holds, leading to an interpretation of average loads $\tilde{M}_z$ and $\tilde{N}_y$ and the auxiliary characteristic length $\tilde{s}_z$.

3.3.2 Choice of Generalized Stresses. In general, the beam nodes are each loaded by three forces and three moments that must satisfy six equilibrium equations. This means that only $12-6=6$ loads are independent; these can be used to define six internal stress measures that solely cause deformation (and no rigid-body motion). Having defined the average loads in Eq. (11), we now specifically choose the generalized stresses: a normal force, a torsion moment, and bending moments at both the ends of the beam

$$\begin{aligned}
\sigma_1&:=\tilde{N}_x, & L\sigma_2&:=\tilde{M}_x\\
L\sigma_3&:=\tilde{M}_y-\tilde{N}_z\tilde{s}_y, & L\sigma_4&:=\tilde{M}_y+\tilde{N}_z(L-\tilde{s}_y)\\
L\sigma_5&:=\tilde{M}_z+\tilde{N}_y\tilde{s}_z, & L\sigma_6&:=\tilde{M}_z-\tilde{N}_y(L-\tilde{s}_z)
\end{aligned} \tag{14}$$

To get the same dimensions (of force) for all σ_i, the moments are scaled with length L. When the displacements are assumed infinitesimal (instead of the finite, but small, displacements considered in the current investigation), these generalized stresses revert to the ones used in the linear analysis of Besseling [28].

3.4 Discrete Deformation Functions. With the definitions of generalized stress $\boldsymbol{\sigma}$ in Eq. (14), expressions for the associated discrete deformations $\boldsymbol{\varepsilon}$ follow from the energy balance in Eq. (10) with Eqs. (11) and (12) as

$$\begin{aligned}
\varepsilon_1&=\int_0^L\gamma_{\bar{x}}\mathrm{d}s, & \varepsilon_2&=L\int_0^L\kappa_{\bar{x}}\mathrm{d}s\\
\varepsilon_3&=\int_0^L[\kappa_{\bar{y}}(L-s)-\gamma_{\bar{z}}]\mathrm{d}s, & \varepsilon_4&=\int_0^L(\kappa_{\bar{y}}s+\gamma_{\bar{z}})\mathrm{d}s\\
\varepsilon_5&=\int_0^L[\kappa_{\bar{z}}(L-s)+\gamma_{\bar{y}}]\mathrm{d}s, & \varepsilon_6&=\int_0^L(\kappa_{\bar{z}}s-\gamma_{\bar{y}})\mathrm{d}s
\end{aligned} \tag{15}$$

Based on geometry, an alternative derivation of these expressions was given by Jonker and Meijaard [21]; the agreement confirms the validity of the current approach, which is instead based on energy conservation to highlight the connection with the original continuum model in Sec. 2. A visualization of deformations ε_1–ε_6 can be found in Boer et al. [29].

Geometric nonlinearities are taken into account by using the second-order expansions of the strain and curvature relations from Eq. (4). With the interpolation functions (Sec. 3.1), the discrete deformations as a function of the nodal coordinates $\boldsymbol{x}$ become

$$\begin{aligned}
\varepsilon_1&=u_x^q+\frac{3}{5L}\left[\left(u_y^q\right)^2+\left(u_z^q\right)^2\right]+\frac{L}{15}\left[\left(\phi_y^q\right)^2+\left(\phi_z^q\right)^2\right]\\
&\quad+\frac{1}{10}\left(\phi_y^q u_z^q-\phi_z^q u_y^q\right)\\
\varepsilon_2&=L\phi_x^q-\frac{L}{2}\phi_y^q\phi_z^q+\phi_y^q u_y^q+\phi_z^q u_z^q\\
\varepsilon_3&=-u_z^q+\frac{L}{6}\phi_x^q\phi_z^q\\
\varepsilon_4&=u_z^q+L\phi_y^q+\phi_x^q\left(-u_y^q+\frac{5}{6}L\phi_z^q\right)\\
\varepsilon_5&=u_y^q-\frac{L}{6}\phi_x^q\phi_y^q\\
\varepsilon_6&=-u_y^q+L\phi_z^q-\phi_x^q\left(u_z^q+\frac{5}{6}L\phi_y^q\right)
\end{aligned} \tag{16}$$

when cubic and higher-order terms are neglected. In accordance with its construction, ε_i shows what the deformed beam looks like

when subjected to generalized stresses σ_i. The quadratic terms are the discrete equivalent of the second-order terms in the finite strain and curvature relations of Eq. (4) of Reissner.

3.5 Equilibrium. According to the principle of virtual work, the generalized stresses are in static equilibrium with the nodal loads if and only if $\boldsymbol{\sigma}^{\mathrm{T}}\delta\boldsymbol{\varepsilon} = \boldsymbol{f}^{\mathrm{T}}\delta\boldsymbol{x}$ holds for all $\delta\boldsymbol{x}$ and $\delta\boldsymbol{\varepsilon}$. Vector $\delta\boldsymbol{x}$ represents the virtual variations of the nodal coordinates $\boldsymbol{x}$ defined in Eq. (7). Quantities $\delta\boldsymbol{x}$ and $\delta\boldsymbol{\varepsilon}$ cannot be varied independently; their relation follows from Eq. (16). The equilibrium condition is expressed as

$$\boldsymbol{\sigma}^{\mathrm{T}}\frac{\partial\boldsymbol{\varepsilon}}{\partial\boldsymbol{x}} = \boldsymbol{f}^{\mathrm{T}} \tag{17}$$

where the nodal loads are collected in $\boldsymbol{f}^{\mathrm{T}} = [\boldsymbol{F}^{\mathrm{T}} \quad \boldsymbol{T}^{\mathrm{T}}]$.

3.6 Stiffness. The discrete analog of the linear constitutive relations of the continuum is derived in a similar fashion to the expressions of the discrete deformations $\boldsymbol{\varepsilon}$, by using the energy balance that is the basis for the discrete model in conjunction with the interpolation functions (Sec. 3.1). The stiffness matrix $\boldsymbol{S} = \mathrm{diag}(S_1, S_2, \boldsymbol{S}_3, \boldsymbol{S}_4)$ has diagonal components

$$\begin{aligned} S_1 &= EA/L, \quad S_2 = GJ/L^3 \\ \boldsymbol{S}_3 &= \frac{EI_y}{(1+\Phi_z)L^3}\begin{bmatrix} 4+\Phi_z & -2+\Phi_z \\ -2+\Phi_z & 4+\Phi_z \end{bmatrix} \\ \boldsymbol{S}_4 &= \frac{EI_z}{(1+\Phi_y)L^3}\begin{bmatrix} 4+\Phi_y & -2+\Phi_y \\ -2+\Phi_y & 4+\Phi_y \end{bmatrix} \end{aligned} \tag{18}$$

and relates the discrete deformations $\boldsymbol{\varepsilon}$ to the generalized stresses $\boldsymbol{\sigma} = \boldsymbol{S}\boldsymbol{\varepsilon}$.

4 Case Study: Lateral Support Stiffness

A flexure strip is represented by the discrete model that was presented in Sec. 3. Since this model captures important spatially deforming flexure strip attributes, it can be used to model a wide variety of flexure mechanisms. In this section, the lateral support stiffness of a flexure strip will be investigated as a case study and a validation.

Node p is fixed and node q is loaded by forces F_y^q and F_z^q in the y- and z-directions. These forces are defined in the global frame, meaning that their orientation does not change when the strip deforms. The cross section is oriented such that the translational y-direction corresponds to the DoF and the z-direction to the DoC of the strip, as indicated in Fig. 5. The displacement of node q in the global z-direction, u_z^q, due to the applied forces is studied as it is characteristic for the support stiffness in this direction.

The solution approach is to start with a kinematic examination of the geometric nonlinearities that are involved. Then, equilibrium conditions will be approximated to express the kinematic relation in terms of nodal forces.

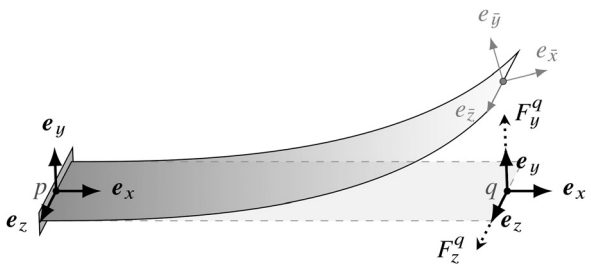

Fig. 5 Discrete model of a flexure strip

4.1 Kinematic Relations. Deformation of the discrete beam model occurs in six modes, termed discrete deformation functions ε_i. They are the discrete analog of the curvature and strain properties for the continuum beam model.

4.1.1 Geometric Nonlinearities. The discrete deformations ε_i are functions of the nodal coordinates $\boldsymbol{x}$. Due to the inclusion of terms that are quadratic in the nodal coordinates, the set of discrete deformations captures geometric nonlinearities relevant to the support stiffness of spatially deformed flexure strips. By expressing the z-direction displacement of node q, u_z^q, in terms of the discrete deformations (essentially solving the ε_i for u_z^q), this effect is taken into account.

4.1.2 Combination of Discrete Deformation Functions. The functional dependencies of ε_i on the nodal coordinates are given by Eq. (16). Discrete deformation ε_3 is important, because it has a first-order contribution of displacement u_z^q, which we are interested in. From this, it follows that u_z^q has a second-order contribution from the twist angle ϕ_x and bending angle ϕ_z in node q. These can be replaced by the corresponding ε_i from Eq. (16) by noting that

$$\varepsilon_2 \approx L\phi_x^q, \quad \varepsilon_5 \approx u_y^q, \quad \varepsilon_6 \approx -u_y^q + L\phi_z^q$$

to first order. The z-direction displacement of node q then becomes

$$u_z^q = -\varepsilon_3 + \frac{1}{6L}\varepsilon_2(\varepsilon_5 + \varepsilon_6) \tag{19}$$

where the cubic and higher terms in ε_i have been omitted.

4.1.3 Interpretation. This specific combination of discrete deformation functions is based purely on kinematic relations and illustrates how the flexure strip deforms to cause displacement of node q in the z-direction. The first-order contribution is ε_3, representing bending in the (x, z)-plane. The second-order contribution is a combination of mode ε_2 and $\varepsilon_5 + \varepsilon_6$, representing the nonlinearity of combined torsion and bending in the (x, y)-plane.

4.1.4 Discretization Error. The use of a discrete model for representing the flexure strip in this analytical investigation can induce a discretization error that stems from interpolation. This error can be identified by means of the numeric implementation of the finite element (see Sec. 3 introduction) that the discrete model is based on—the spatial beam finite element in the numeric flexible multibody software SPACAR [13]. In this software, multiple elements can be interconnected to represent beamlike mechanisms in various static and dynamic simulations.

When a single such finite element is used and subjected to the same boundary conditions as the presented discrete model, it has the same static behavior. By then increasing the number of finite elements representing a single flexure strip (i.e., reducing the element size) in the numeric simulation, the accuracy of the solution improves and the discretization error can be identified.

Given that calculations involving torsion have a limited order of convergence when the torsion angle is approximated only linearly, care is taken to check how accurate a single element describes the torsional deformation.

The lateral support stiffness, defined as F_z^q/u_z^q, is calculated numerically for a flexure strip with dimensions 80 mm × 32 mm × 0.8 mm and Young's modulus 210 GPa, as a function of the dimensionless DoF-displacement u_y^q/L. By increasing the number of elements that make up the strip, the discretization error becomes apparent, as indicated in Fig. 6(*a*): when using only a single element, the stiffness differs considerably from the converged solution (represented by 20 elements).

The need to use multiple elements for representing this deformation behavior can be attributed to the interpolation of the twist angle. As detailed in Sec. 3.1, the interpolation is only linear

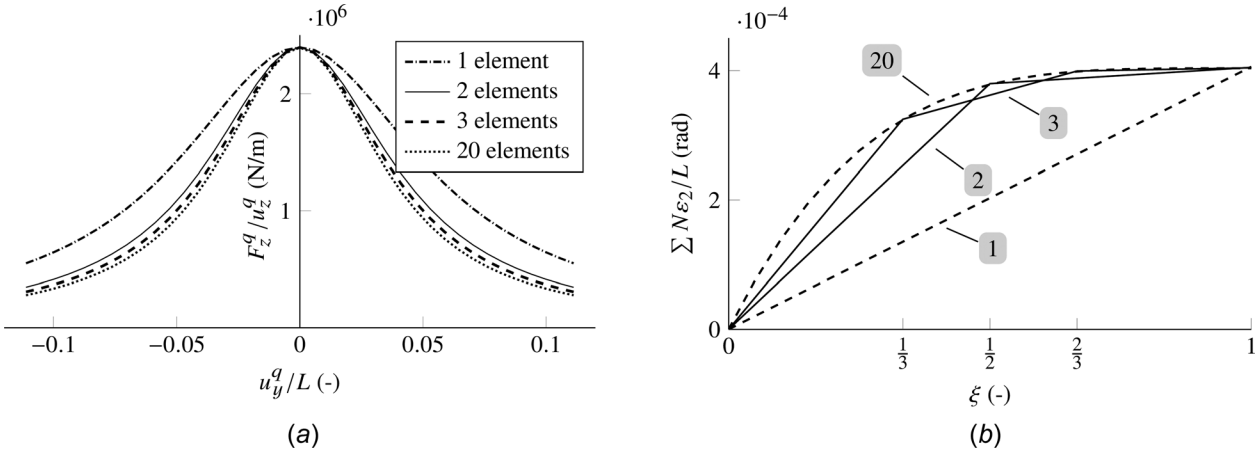

Fig. 6 Effect of decreasing element size (the use of multiple elements per flexure strip means that the element size reduces). (*a*) Lateral support stiffness and (*b*) cumulative angle of twist.

between the rotations in the nodes. From a numeric simulation, this twist angle can be calculated by means of the second discrete deformation function ε_2, which represents torsion deformation. According to Eq. (16), their relation to first order is $\phi_x^q \approx N\varepsilon_2/L$, where N represents the number of elements that are used.

For an increasing number of elements, Fig. 6(*b*) shows the twist angle as a function of the dimensionless coordinate along the beam $\xi = s/L$. Clearly, the piecewise linear contributions of each element converge to a twist angle function that is significantly different from the one-element solution. While all the simulations return the same twist angle at the end ($\xi = 1$), the twist angle behavior in particular near the midsection of the flexure strip is not captured well by a single element, explaining the need for multiple elements when torsion is involved.

4.2 Improved Torsion Interpolation. For the specific case of deformation in lateral support direction, the torsional accuracy of the element can be improved by refining the interpolation of the twist angle, though this will come at a loss of general applicability. The functions that interpolate between nodal coordinates $\boldsymbol{x}$ are involved in the derivation of the discrete deformation functions ε_i. This is evidenced by the integral expressions of ε_i in Eq. (15) in conjunction with strain and curvature relations in Eq. (4). A change in interpolation functions will therefore lead to different expressions for the discrete deformation functions in terms of the nodal coordinates, meaning that Eq. (16) no longer holds.

The twist angle $\phi_x(\xi)$ is related to the internal torsion moment $M_{\bar{x}}(\xi)$ via the specific twist angle $\kappa_{\bar{x}}(\xi)$ and the constitutive model $M_{\bar{x}} = GJ\kappa_{\bar{x}}$ from Eq. (5). From the results of a linear analysis of the displacements that contribute to $M_{\bar{x}}$, a more accurate ϕ_x can be obtained. This will be detailed in this section.

Due to the flexure strip geometry, displacement u_y^q (the translational DoF) is much larger than u_z^q (a DoC) under practical load cases. The contribution of u_z^q to $M_{\bar{x}}$ is therefore neglected. Figure 7 shows the deformed shape of the flexure strip in the (x, y)-plane. As a consequence of the deflected shape, the internal torsion moment (directed along the tangent of the elastic line) consists of contributions from global moments $M_x(\xi)$ and $M_y(\xi)$, according to

$$M_{\bar{x}}(\xi) = M_x(\xi)\cos(\phi_z) + M_y(\xi)\sin(\phi_z) \approx M_x(\xi) + M_y(\xi)\frac{1}{L}\frac{\mathrm{d}u_y}{\mathrm{d}\xi} \quad \text{for small } \phi_z \tag{20}$$

Moment $M_x(\xi)$ about the global x-axis is caused by displacement u_y^q in conjunction with force F_z^q

$$M_x(\xi) = F_z^q(u_y^q - u_y(\xi)) \tag{21}$$

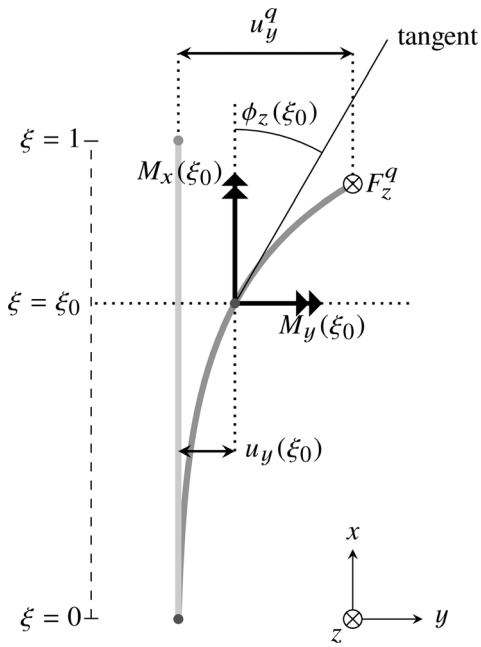

Fig. 7 Contributions to torsion moment $M_{\bar{x}}(\xi)$, directed along the elastic line tangent

clearly showing the contribution of the deformed shape $u_y(\xi)$. This shape can be expressed using the results of a linear analysis of the transverse displacement of a fixed–free beam subject to an end-force only, as

$$u_y(\xi) = u_y^q\left(\frac{3}{2}\xi^2 - \frac{1}{2}\xi^3\right) \tag{22}$$

Moment $M_y(\xi)$ about the global y-axis is also caused by F_z^q and varies linearly over the beam length

$$M_y(\xi) = F_z^q(\xi - 1)L \tag{23}$$

Substitution of Eqs. (21)–(23) into Eq. (20) yields

$$M_{\bar{x}}(\xi) = F_z^q u_y^q(1 - 3\xi + 3\xi^2 - \xi^3) \tag{24}$$

which is the interpolation of the internal torsion moment using a cubic polynomial based on the results of linear deflection analysis. The twist angle then follows as:

$$\phi_x(\xi) = L\int_{\bar{\xi}=0}^{\xi} \kappa_{\bar{x}}(\bar{\xi})\mathrm{d}\bar{\xi} = \frac{L}{GJ}\int_0^{\xi} M_{\bar{x}}(\bar{\xi})\mathrm{d}\bar{\xi}$$
$$= \frac{L}{GJ}F_z^q u_y^q\left(\xi - \frac{3}{2}\xi^2 + \xi^3 - \frac{1}{4}\xi^4\right) \tag{25}$$

and is visually indistinguishable from the numeric 20-element twist angle in Fig. 6(*b*). While this interpolation function is now a quartic polynomial, instead of the conventional linear polynomial (Sec. 3.1), it is no longer general and only applicable to this specific torsion problem.

The discrete deformation functions ε_i in terms of nodal coordinates $\boldsymbol{x}$, Eq. (16), are affected by the refined ϕ_x. From the integral expressions of ε_i in Eq. (15), which are independent of interpolation, it can be seen that primarily ε_2 is affected, because its integrand is simply the specific twist angle $\kappa_{\bar{x}}$. Since ε_2 is a measure for torsion deformation, this makes sense.

As was seen in the derivation of the z-direction displacement in Eq. (19), bending measures ε_3, ε_4, ε_5, and ε_6 have a second-order contribution from torsion and are affected as well: the continuous curvature relations in Eq. (4) show that bending curvatures $\kappa_{\bar{y}}$ and $\kappa_{\bar{z}}$ consist of a second-order term that involves ϕ_x.

4.3 Revised Kinematic Relations. Discrete deformation function ε_3, given by Eq. (15), can be evaluated using Eq. (4) and the refined ϕ_x to give

$$\varepsilon_3 = -u_z^q + \frac{1}{7}\frac{L}{GJ}F_z^q\left(u_y^q\right)^2$$

Compared to the original expression in Eq. (16), the first-order term has not changed. Note that, as before, $\varepsilon_5 \approx u_y^q$ to first order, the z-direction displacement of node q now becomes

$$u_z^q = -\varepsilon_3 + \frac{1}{7}\frac{L}{GJ}F_z^q(\varepsilon_5)^2 \tag{26}$$

4.4 Material Stiffness and Equilibrium

4.4.1 Generalized Stresses. As per their construction in Sec. 3.2, the discrete deformations $\boldsymbol{\varepsilon}$ and the generalized stresses $\boldsymbol{\sigma}$ have an explicit linear relation. It is given by $\boldsymbol{\sigma} = \boldsymbol{S}\boldsymbol{\varepsilon}$ and $\boldsymbol{\varepsilon} = \boldsymbol{S}^{-1}\boldsymbol{\sigma}$ for the stiffness matrix $\boldsymbol{S}$ of Sec. 3.6. This relation can be used to express the relevant ε_i in Eq. (26) in terms of σ_i as

$$u_z^q = -\left(\frac{\sigma_3}{\tilde{S}_{3,3}} + \frac{\sigma_4}{\tilde{S}_{3,4}}\right) + \frac{1}{7}\frac{L}{GJ}F_z^q\left(\frac{\sigma_5}{\tilde{S}_{5,5}} + \frac{\sigma_6}{\tilde{S}_{5,6}}\right)^2 \tag{27}$$

where $1/\tilde{S}_{i,j}$ is the i,jth component of matrix $\boldsymbol{S}^{-1}$.

4.4.2 Equilibrium Equations. Equilibrium (Sec. 3.5) between the generalized stresses and nodal loads is governed by Eq. (17). Jacobian matrix $(\partial\boldsymbol{\varepsilon}/\partial\boldsymbol{x})$ consists of derivatives of the discrete deformations $\boldsymbol{\varepsilon}$ in Eq. (16) with respect to the nodal coordinates $\boldsymbol{x}$ in Eq. (7). This means that equilibrium between $\boldsymbol{\sigma}$ and $\boldsymbol{f}$ is dependent on the configuration (given by the nodal coordinates $\boldsymbol{x}$) of the element. By approximating the deformed configuration with

$$u_x^q = 0, \quad |u_y^q| < L/10, \quad u_z^q = 0$$

it can be shown that Eq. (17) leads to

$$\begin{aligned} \sigma_3 &\approx -F_z^q, & \sigma_4 &= 0 \\ \sigma_5 &\approx F_y^q, & \sigma_6 &= 0 \end{aligned} \tag{28}$$

When $\sigma_6 = 0$, it follows that $\varepsilon_5 \approx \sigma_5/\tilde{S}_{5,5}$, so that

$$\sigma_5 \approx \tilde{S}_{5,5}\varepsilon_5 \approx \tilde{S}_{5,5}u_y^q \tag{29}$$

With Eqs. (27)–(29), the z-direction displacement in terms of nodal loads and coordinates becomes

$$u_z^q = F_z^q\left(\frac{L^3}{3EI_y} + \frac{L}{k_zGA} + \frac{L}{7GJ}\left(u_y^q\right)^2\right) \tag{30}$$

The lateral support stiffness of the flexure strip is

$$\frac{F_z^q}{u_z^q} = \left(\frac{L^3}{3EI_y} + \frac{L}{k_zGA} + \frac{L}{7GJ}\left(u_y^q\right)^2\right)^{-1}$$

This expression shows a bending, shearing, and torsion term, respectively. The bending and shearing term depend only on material and geometric parameters and would also be captured in a linearized analysis. The torsion term, though, is quadratically dependent on DoF-displacement u_y^c and only captured in this nonlinear analysis. The corresponding graph is visually identical to the 20-element graph in Fig. 6(*a*). The significance of this last nonlinear term is that it explicates the undesired decrease in lateral support stiffness that is observed when the flexure strip is deflected in one of its DoF. This expression explains what parameters can be tuned to optimize the lateral support stiffness of a flexure strip *over the range of motion* for a given application.

In certain applications, displacement u_y^q can be greater than $L/10$. In that case, one can pursue a similar modeling approach while making an appropriate truncation assumption for the discrete deformations in Eq. (15).

4.5 Validation Using Prior Art: Extension to a Parallelogram Flexure Mechanism. Load–displacement equation (30) is valid for the elementary fixed–free flexure strip loaded only by forces F_y^q and F_z^q at the free end. In practical mechanisms, however, it is unlikely to find a flexure strip that is not fixed at both ends. This means that in practice, an additional moment M_z^q about the z-axis at the free end is present, enforcing the zero slope boundary condition. As the fixed–free flexure strip of the previous analysis does develop an *internal* moment M_z due to force F_y^q, it can be extended to describe the more common fixed-guided strip. This result in turn can be used to rederive an expression from prior art to serve as a validation of Eq. (30).

Figure 8 shows a parallelogram flexure mechanism, widely used in precision design for approximate straight motion guidance, that consists of two such flexure strips and a shuttle in between. The stiffness in the lateral support direction along the z-axis is studied by displacing the mechanism

- in the DoF along the global y-axis with force F_y^c
- in the DoC along the global z-axis with force F_z^c

They are applied at the nominal center of stiffness, which is located at $L^p/2$ from the ground and in the center of the shuttle.

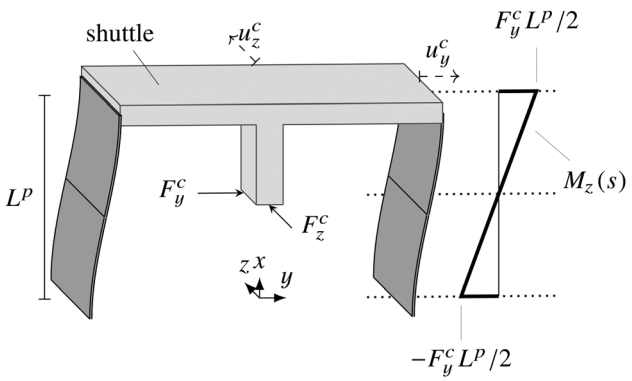

Fig. 8 Parallelogram flexure mechanism. Internal bending moment $M_z(s)$ is shown on the right.

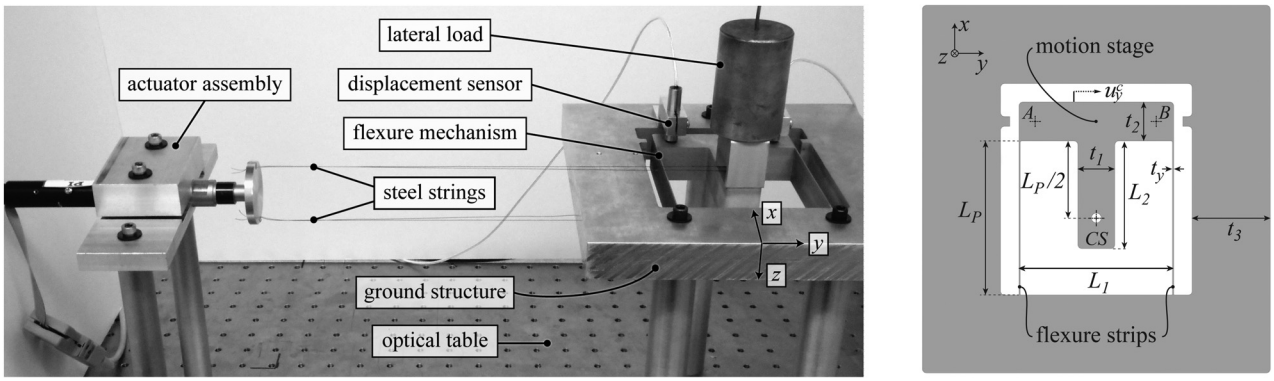

Fig. 9 Experimental setup for measuring the lateral support stiffness: (*a*) full setup and (*b*) parallelogram flexure mechanism

Applying a F_y force at the center of stiffness leads to the least (theoretically zero) parasitic z-axis rotation of the shuttle [27]. Most notably, the internal bending moment M_z developed in the flexure strip about the z-axis displays a symmetry, as indicated in Fig. 8. For this specific load case, it is zero at the midsection ($x = L^p/2$) of the strip. This means that each fixed-guided strip in this mechanism can be represented by a combination of two fixed–free strips of the previous analysis. The deflection of the fixed-guided strip is then simply twice that of the fixed–free strip.

Substitution of the kinematic and force relations

$$L = \frac{1}{2}L^p, \quad u_y^q = \frac{1}{2}u_y^c, \quad u_z^q = \frac{1}{2}u_z^c, \quad F_z^q = \frac{1}{2}F_z^c$$

into Eq. (30) yields the load–displacement relation for the z-direction of this parallelogram flexure mechanism

$$u_z^c = F_z^c\left(\frac{(L^p)^3}{24EI_y} + \frac{L^p}{2k_zGA} + \frac{L^p}{56GJ}\left(u_y^c\right)^2\right) \tag{31}$$

from which the lateral support stiffness follows as F_z^c/u_z^c.

For a validation of the new closed-form modeling approach of the present work, we note that Brouwer et al. [5] have derived Eq. (31) using a different approach, based on an ad hoc continuum model specific to a parallelogram configuration. The expression has been extensively validated for various geometric parameters controlling the shear and torsion, against finite-element analysis within 6.0% error for $u_y^c = 0.1L^p$ and 13.9% for displacements as large as $u_y^c = 0.3L^p$.

Their analysis also takes into account constrained cross-sectional warping [30], which manifests as an effective torsional stiffness increase when both ends of the flexure strip are clamped. For an accurate prediction of the torsional stiffness in the validating experiment of Sec. 5, the effect is noted here. It can be accounted for by simply dividing the torsional stiffness GJ by a factor

$$1 + \frac{588}{5\lambda^2} + \frac{2688}{\lambda^4} + \frac{16128}{\lambda^6} - \left(\frac{14}{\lambda} + \frac{672}{\lambda^3} + \frac{8064}{\lambda^5}\right)\coth\left(\frac{1}{2}\lambda\right)$$

where dimensionless spatial decay rate λ, independent of deformation, is given by

$$\lambda = L^p\sqrt{\frac{GJ}{\Gamma E}} \quad \text{with} \quad \Gamma \approx \frac{1}{144}t_y^3t_z^3$$

Parameter Γ represents the warping constant, t_y the thickness, and t_z the width of the flexure strip.

5 Experimental Validation

An experiment has been conducted to validate the analytical stiffness model, by measuring the actual lateral *deflection* u_z^c under a lateral force F_z^c as a function of translational DoF u_{yc}.

5.1 Materials. The experimental setup (Fig. 9(*a*)) consists of a ground structure with flexure mechanism, actuator assembly, lateral load, and lateral displacement sensors.

The parallelogram flexure mechanism and ground structure are made from a 26.0 mm thick plate of AL6061 material using wire electrical discharge machining. Table 2 shows relevant dimensions that are indicated in Fig. 9(*b*). These dimensions yield a compact desktop assembly that is easy to manufacture and capable of showing the geometrically nonlinear compliance contribution from torsion of the flexure strips.

The maximum displacement in DoF u_y^c is 6 mm in both directions while staying within 40% of the yield strength. The motion stage has a T-shape to accommodate the center of stiffness (CS), where the lateral force F_z^c and the actuation force F_y^c are applied.

5.1.1 Actuation, Loading, and Sensing. The flexure mechanism requires an F_y^c actuation force of 9 N for a stroke of ±6 mm. These requirements are met by a DC motor-driven nonrotating tip precision micrometer (PhysikInstrumente, M-227.25) with a positioning accuracy of 2 μm.

The actuator and flexure mechanism are connected by strings, since strings do not resist the lateral motion of the mechanism. Two strings are used to create a resultant force F_y^c at the CS that should minimize rotation about the x-axis.

Lateral load F_z^c is applied by means of a 1 kg weight placed on a platform weighing 48 g. Displacement u_z^c and the stage rotation about the x-axis are measured by two capacitance probes (Lion Precision, C-1A), located as far apart as possible at points A and B in Fig. 9(*b*). Because of the high accuracy of the probes (19.2 nm total uncertainty), the associated measurement error in u_z^c is only 0.2% at most and neglected. A real-time control prototyping system (dSPACE, DS1103) is used to control the DoF actuator and to acquire and store data from the capacitance probes.

Table 2 Dimensions (mm) indicated in Fig. 9(*b*)

L_P	t_y	t_z	L_1	L_2	t_1	t_2	t_3
100.0	0.78	26.0	100	70	25.4	24	50.8

5.2 Methods

5.2.1 Experimental Procedure. The flexure mechanism is displaced from $u_y^c = 0$ to 6 mm in steps of 0.5 mm with a dwell time of 30 s at each position. The lateral displacement as measured by the capacitance probes is recorded at each position. This process is repeated for the mechanism loaded by the platform and weight, and for the negative displacement range, by switching the entire actuator assembly to the other side of the mechanism.

5.2.2 Analysis Techniques. The lateral displacement u_z^c is obtained as the average of the two capacitance probe readings. In accordance with the analytical model in Eq. (31), the measurement data of u_z^c at the positions u_y^c are fitted to a quadratic model with structure

$$u_z^c = c_2(u_y^c - c_1)^2 + c_0 \tag{32}$$

While the analytical model lacks a term linear in u_y^c, it is included in this regression model by means of coefficient c_1 to account for any string slack or play in the absence of tension, which may result in a starting position that does not exactly match the true zero condition (i.e., zero deformation) of the mechanism. The MATLAB curve fitting toolbox is used to perform the nonlinear least squares optimization and calculate goodness-of-fit statistics.

As the discussed error sources that stem from actuation and sensing are expected to be negligibly small, the main discrepancy between measured and predicted coefficients will be due to theoretical idealizations and uncertainty in the measurement of the mechanism dimensions (especially in the presence of manufacturing imperfections). The analytical model is a function of four measured quantities and approximately affected by their uncertainties according to

$$\Delta u_z^c \approx \frac{\partial u_z^c}{\partial F_z^c}\Delta F_z^c + \frac{\partial u_z^c}{\partial L^p}\Delta L^p + \frac{\partial u_z^c}{\partial t_y}\Delta t_y + \frac{\partial u_z^c}{\partial t_z}\Delta t_z \tag{33}$$

in conjunction with the datasheet accuracy values in Table 3.

5.3 Results. Figure 10 shows the measurement data, along with the regression fit and theoretical prediction. The experiment value and theoretical prediction of the coefficients are summarized in Table 4. The regression coefficients are reliably estimated according to the goodness-of-fit statistics (adjusted R-square 0.997 and root mean squared error 5×10^{-8}). The uncertainty in u_z^c due to measurement accuracy is estimated with Eq. (33) to be at most 4.7% over the displacement range in the y-direction.

Coefficient c_1 is estimated with confidence bounds that cross zero, suggesting that it does not significantly differ from zero. This means that the measurement is not affected by string slack or play in the absence of tension. From the measurements of the two separated z-direction displacement sensors, the stage rotation about the x-axis, caused by the string actuation, is estimated to affect u_z^c by 1.2% at most and therefore neglected.

The prediction of coefficient c_2 matches very well with the experiment result. This indicates that the nonlinear dependency on displacement in the DoF is captured by the analytical model. The deviation between the prediction and experiment value of coefficient c_0 is considerable, though. Qualitatively, the theory overpredicts the z-direction stiffness of the mechanism in the initial configuration (when $u_y^c = 0$).

Table 3 Accuracy of measured quantities

Quantity	Device	Symbol	Accuracy
Weight	Scale	ΔF_z^c	14 mN
Strip length	Caliper	ΔL^p	25 μm
Strip width	Caliper	Δt_z	25 μm
Strip thickness	Disk micrometer	Δt_y	23 μm

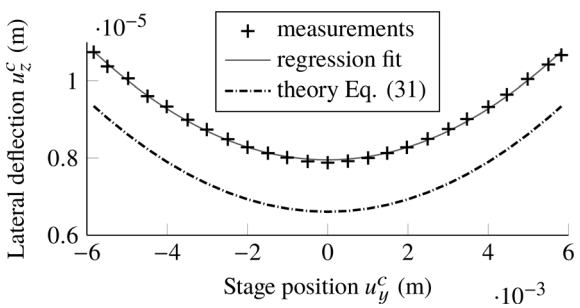

Fig. 10 Experimental and theoretical results

Table 4 Comparison of analytical and experimental results

Coefficient	Experiment	Theory	Deviation (%)
$c_0 \cdot 10^6$	7.95	6.60	20.5
$c_2 \cdot 10^2$	8.28	8.08	2.4

5.4 Discussion. Potential error sources are the placement of the weight and unmodeled compliance due to assumptions on rigidity and ideal flexure strip geometry. In this section, these sources are discussed. Where numeric validation is mentioned, the flexible multibody software SPACAR [13], discussed in Sec. 4.1.4, was used.

Placement of weight F_z^c that is off in y-direction by 1.5 mm (which would be visible) has been numerically calculated to have a negligible effect on u_z^c.

The T-shaped section of the motion stage can be regarded as a fixed–free short beam with dimensions $L_p/2 \times t_1 \times t_z$ (Table 2) subjected to end-load F_z^c. Its bending and shear deformation contribute around 0.2 μm to u_z^c, affecting c_0 with approximately 3%.

It is likely that the assumptions of ideal flexure strip geometry and boundary conditions in the analytical model are violated, adding compliance in the z-direction. Because this compliance is independent of the y-direction displacement, it presents as a discrepancy solely in coefficient c_0. This highlights the significance of the presentation of the results in two coefficients: while c_0 captures the main discrepancy between experiment and theory, c_2 still captures the geometrically nonlinear torsion effect of interest very accurately.

The effect of geometric imperfections, caused by, e.g., materials relieving their internal stress upon machining, is investigated by means of flexure strips that have a quadratic instead of straight shape in the initial configuration, as shown in Fig. 11. The maximum deflection u_y^i is a measure for nonideal geometry in the (x, y)-plane of the flexure strip. A numeric sensitivity analysis has shown that a deflection of $u_y^i = 3.5t_y$ could explain the discrepancy in coefficient c_0. While this particular beam shape only serves as a proxy for the actual flexure strip imperfection, it clearly shows how geometry variations can significantly undermine the lateral support stiffness in the initial configuration. In reality, the flexure strips will have distortions to some degree in both in-plane and out-of-plane directions. Together with other inaccuracies in the construction, we expect that these account for the present deviation in coefficient c_0 between theory and experiment.

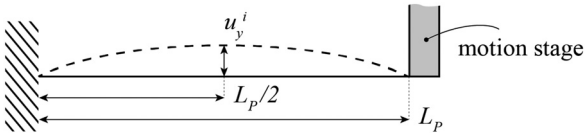

Fig. 11 Nonideal flexure strip geometry, governed by u_y^i

6 Conclusion

This paper has presented the foundation and a validation of a new approach for obtaining closed-form expressions that model the nonideal constraint behavior of spatially deforming flexure strips. The details of a suitable discretized static beam model have been presented. Based on the finite-element assumptions on interpolation, the discrete model facilitates analytical calculations. As a case study, the decreasing lateral support stiffness that accompanies deformation in the intended degree of freedom (DoF) has been studied for a parallelogram flexure mechanism. It has been shown that this performance-decreasing compliance is governed by a geometrically nonlinear contribution due to torsion and quadratically dependent on the transverse DoF displacement. The resulting lateral stiffness expression has experimentally been validated and shown to provide parametric insight with sufficient accuracy for a geometry and load range of practical interest.

References

[1] Jones, R. V., 1956, "A Parallel-Spring Cross-Movement for an Optical Bench," J. Sci. Instrum., **33**(7), pp. 279–280.

[2] Howell, L. L., Magleby, S. P., and Olsen, B. M., 2013, *Handbook of Compliant Mechanisms*, Wiley, Chichester, UK.

[3] Blanding, D. L., 1999, *Exact Constraint: Machine Design Using Kinematic Principles*, ASME Press, New York.

[4] Awtar, S., Slocum, A. H., and Sevincer, E., 2007, "Characteristics of Beam-Based Flexure Modules," ASME J. Mech. Des., **129**(6), pp. 625–639.

[5] Brouwer, D. M., Meijaard, J. P., and Jonker, J. B., 2013, "Large Deflection Stiffness Analysis of Parallel Prismatic Leaf-Spring Flexures," Precis. Eng., **37**(3), pp. 505–521.

[6] Zelenika, S., and De Bona, F., 2002, "Analytical and Experimental Characterisation of High-Precision Flexural Pivots Subjected to Lateral Loads," Precis. Eng., **26**(4), pp. 381–388.

[7] Sen, S., 2013, "Beam Constraint Model: Generalized Nonlinear Closed-Form Modeling of Beam Flexures for Flexure Mechanism Design," Ph.D. thesis, University of Michigan, Ann Arbor, MI.

[8] Awtar, S., and Sen, S., 2010, "A Generalized Constraint Model for Two-Dimensional Beam Flexures: Nonlinear Load-Displacement Formulation," ASME J. Mech. Des., **132**(8), p. 081008.

[9] Sen, S., and Awtar, S., 2013, "A Closed-Form Nonlinear Model for the Constraint Characteristics of Symmetric Spatial Beams," ASME J. Mech. Des., **135**(3), p. 11.

[10] Rasmussen, N. O., Wittwer, J. W., Todd, R. H., Howell, L. L., and Magleby, S. P., 2006, "A 3D Pseudo-Rigid-Body Model for Large Spatial Deflections of Rectangular Cantilever Beams," ASME Paper No. DETC2006-99465.

[11] Ramirez, I. A., and Lusk, C. P., 2011, "Spatial-Beam Large-Deflection Equations and Pseudo-Rigid-Body Model for Axisymmetric Cantilever Beams," ASME Paper No. DETC2011-47389.

[12] Meijaard, J. P., 2011, "Refinements of Classical Beam Theory for Beams With a Large Aspect Ratio of Their Cross-Sections," IUTAM Symposium on Dynamics Modeling and Interaction Control in Virtual and Real Environments, Budapest, Hungary, June 7–11, pp. 285–292.

[13] Jonker, J. B., and Meijaard, J. P., 1990, "SPACAR—Computer Program for Dynamic Analysis of Flexible Spatial Mechanisms and Manipulators," *Multibody Systems Handbook*, W. Schiehlen, ed., Springer, Berlin, pp. 123–143.

[14] Meijaard, J. P., Brouwer, D. M., and Jonker, J. B., 2010, "Analytical and Experimental Investigation of a Parallel Leaf Spring Guidance," Multibody Syst. Dyn., **23**(1), pp. 77–97.

[15] Brouwer, D. M., Folkersma, K. G. P., Boer, S. E., and Aarts, R. G. K. M., 2013, "Exact Constraint Design of a Two-Degree of Freedom Flexure-Based Mechanism," ASME J. Mech. Rob., **5**(4), p. 041011.

[16] Wijma, W., Boer, S. E., Aarts, R. G. K. M., Brouwer, D. M., and Hakvoort, W. B. J., 2014, "Modal Measurements and Model Corrections of a Large Stroke Compliant Mechanism," Arch. Mech. Eng., **61**(2), pp. 347–366.

[17] Cosserat, E., and Cosserat, F., 1909, *Théorie des Corps Déformables*, Librairie Scientifique A. Hermann et Fils, Paris, France.

[18] Lang, H., Linn, J., and Arnold, M., 2011, "Multi-Body Dynamics Simulation of Geometrically Exact Cosserat Rods," Multibody Syst. Dyn., **25**(3), pp. 285–312.

[19] Cowper, G. R., 1966, "The Shear Coefficient in Timoshenko's Beam Theory," ASME J. Appl. Mech., **33**(2), pp. 335–340.

[20] Goldstein, H., Poole, C., and Safko, J., 2001, *Classical Mechanics*, 3rd ed., Addison-Wesley, Boston, MA.

[21] Jonker, J. B., and Meijaard, J. P., 2013, "A Geometrically Non-Linear Formulation of a Three-Dimensional Beam Element for Solving Large Deflection Multibody System Problems," Int. J. Non-Linear Mech., **53**, pp. 63–74.

[22] Reissner, E., 1973, "On One-Dimensional Large-Displacement Finite-Strain Beam Theory," Stud. Appl. Math., **52**(2), pp. 87–95.

[23] Irschik, H., and Gerstmayr, J., 2011, "A Continuum-Mechanics Interpretation of Reissner's Non-Linear Shear-Deformable Beam Theory," Math. Comput. Modell. Dyn. Syst., **17**(1), pp. 19–29.

[24] Simo, J. C., and Vu-Quoc, L., 1986, "On the Dynamics of Flexible Beams Under Large Overall Motions—The Plane Case: Part I," ASME J. Appl. Mech., **53**(4), pp. 849–854.

[25] Nachbagauer, K., Pechstein, A. S., Irschik, H., and Gerstmayr, J., 2011, "A New Locking-Free Formulation for Planar, Shear Deformable, Linear and Quadratic Beam Finite Elements Based on the Absolute Nodal Coordinate Formulation," Multibody Syst. Dyn., **26**(3), pp. 245–263.

[26] Przemieniecki, J. S., 1968, *Theory of Matrix Structural Analysis*, McGraw-Hill, New York.

[27] Awtar, S., 2004, "Synthesis and Analysis of Parallel Kinematic XY Mechanisms," Sc.D. thesis, Massachusetts Institute of Technology, Cambridge, MA.

[28] Besseling, J. F., 1974, "Non-Linear Analysis of Structures by the Finite Element Method as a Supplement to a Linear Analysis," Comput. Methods Appl. Mech. Eng., **3**(2), pp. 173–194.

[29] Boer, S. E., Aarts, R. G. K. M., Meijaard, J. P., Brouwer, D. M., and Jonker, J. B., 2014, "A Nonlinear Two-Node Superelement for Use in Flexible Multibody Systems," Multibody Syst. Dyn., **31**(4), pp. 405–431.

[30] Timoschenko, S., 1922, "On the Torsion of a Prism, One of the Cross-Sections of Which Remains Plane," Proc. London Math. Soc., **20**(1), pp. 389–397.